Bayesian Nonparametrics for FRET using Realistic Integrative Detectors

Ayush Saurabh[1,2], Gde Bimananda Mahardika Wisna[1,2,3], Maxwell Schweiger[1,2], Rizal Hariadi[1,2,3], and Steve Pressé[1,2,4,*]

[1]Center for Biological Physics, Arizona State University, Tempe, AZ, USA
[2]Department of Physics, Arizona State University, Tempe, AZ, USA
[3]Center for Molecular Design and Biomimetics at the Biodesign Institute, Arizona State University, Tempe, AZ, USA.
[4]School of Molecular Sciences, Arizona State University, Tempe, AZ, USA
[*]spresse@asu.edu

August 27, 2025

Abstract

Förster resonance energy transfer (FRET) is a widely used tool to probe nanometer scale dynamics, projecting rich 3D biomolecular motion onto noisy 1D traces. However, interpretation of FRET traces remains challenging due to degeneracy—distinct structural states map to similar FRET efficiencies—and often suffers from under- and/or over-fitting due to the need to predefine the number of FRET states and noise characteristics. Here we provide a new software, Bayesian nonparametric FRET (BNP-FRET) for binned data obtained from integrative detectors, that eliminates user-dependent parameters and accurately incorporates all known noise sources, enabling the identification of distinct configurations from 1D traces in a plug-n-play manner. Using simulated and experimental data, we demonstrate that BNP-FRET eliminates logistical barrier of predetermining states for each FRET trace and permits high-throughput, simultaneous analysis of a large number of kinetically heterogeneous traces. Furthermore, working in the Bayesian paradigm, BNP-FRET naturally provides uncertainty estimates for all model parameters including the number of states, kinetic rates, and FRET efficiencies.

Main

Förster resonance energy transfer (FRET) has served as a spectroscopic ruler to study the motion of biomolecules at the nanometer scale [1, 2, 3, 4], and has revealed insights into intra- and intermolecular dynamics of proteins [5, 6, 7, 8, 9, 10, 11], nucleic acids [12], and their interactions [13, 14]. Such motion is usually tracked from changes in the FRET signal obtained from two light-emitting fluorescent molecules, called donor and acceptor, attached to the biomolecule of interest. During experiments, the donor is typically excited with a laser, and then both donor and acceptor emit light at rates determined by the distance between them. The distance R is determined from the donor and acceptor emission rates, n_D and n_A, using the following expression

$$E^{FRET} = \frac{n_A}{n_A + n_D} = \frac{1}{1 + (R/R_0)^6},$$

where E^{FRET} is the FRET efficiency, and R_0 is the distance at which the energy transfer is half-maximum ($E^{FRET} = 0.5$), termed as the Föster radius.

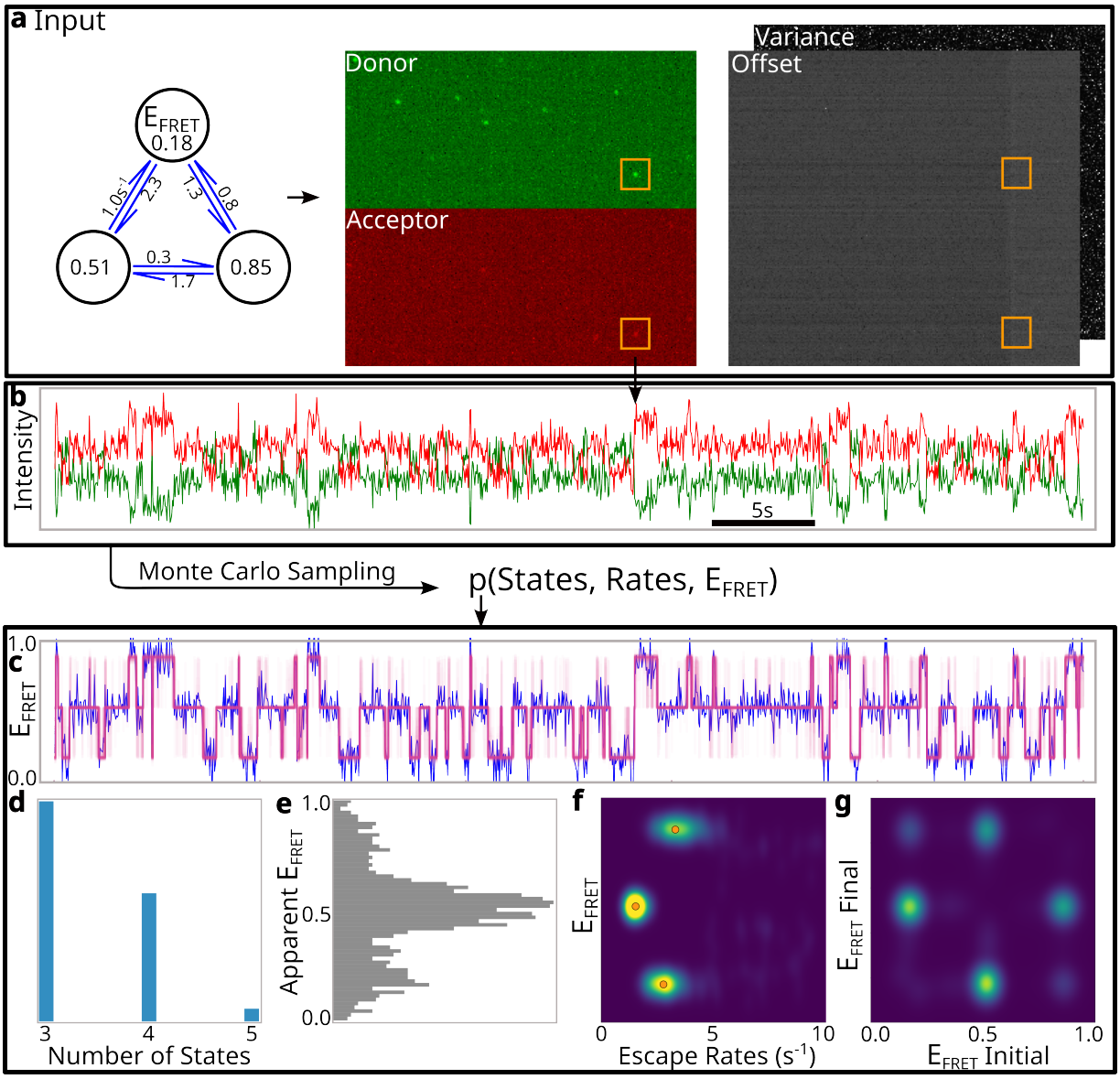

Fig. 1: BNP-FRET analysis of a simulated 3-state FRET trace. a. The kinetics of biomolecules are observed under a microscope using a camera. The two camera channels for donor and acceptor fluorescence see diffraction-limited spots at the same locations as highlighted using orange squares. Camera noise calibration maps for readout offset and variance are used to compute background emissions and characterize noise properties for state identification. **b.** The FRET time trace shown is produced by integrating intensities recorded at pixels in the small square neighborhood around the particle shown in the orange squares in a. Monte Carlo samples are then generated by BNP-FRET to estimate a probability distribution over states, kinetic rates, and FRET efficiencies. **c.** Distribution over state trajectories shown in pink as generated using 200 samples. Apparent FRET efficiency directly computed from data is shown in blue. **d.** Histogram over estimated number of states. The 3 state model is most dominant. Noise in data implies high number of states may be estimated in some samples. **e.** Apparent FRET efficiency histogram shows most of the time is spent in the intermediate FRET efficiency state. **f.** FRET efficiency vs escape rates (sum of all outgoing rates from a state) probability distribution. The ground truth is shown with orange dots. **g.** Transition density plots showing that most transitions occur in and out of the intermediate FRET efficiency state as expected.

Since the distance between the fluorescent molecules only provides one-dimensional information, iden-

tifying 3D changes in configurations or states of the biomolecules from FRET time traces is an open challenge. The difficulty of identifying states is further compounded by photon shot noise, detector noise, background, spectral crosstalk, and imperfections of fluorescence emission. However, commonly available FRET analysis tools either make Gaussian assumptions about the noise in FRET data, do not calibrate pixel-to-pixel varying detector noise, and require fixing the number of states in advance [15, 16] in the case of unsupervised tools, or require expensive training on simulated data in the case of supervised tools [17, 18].

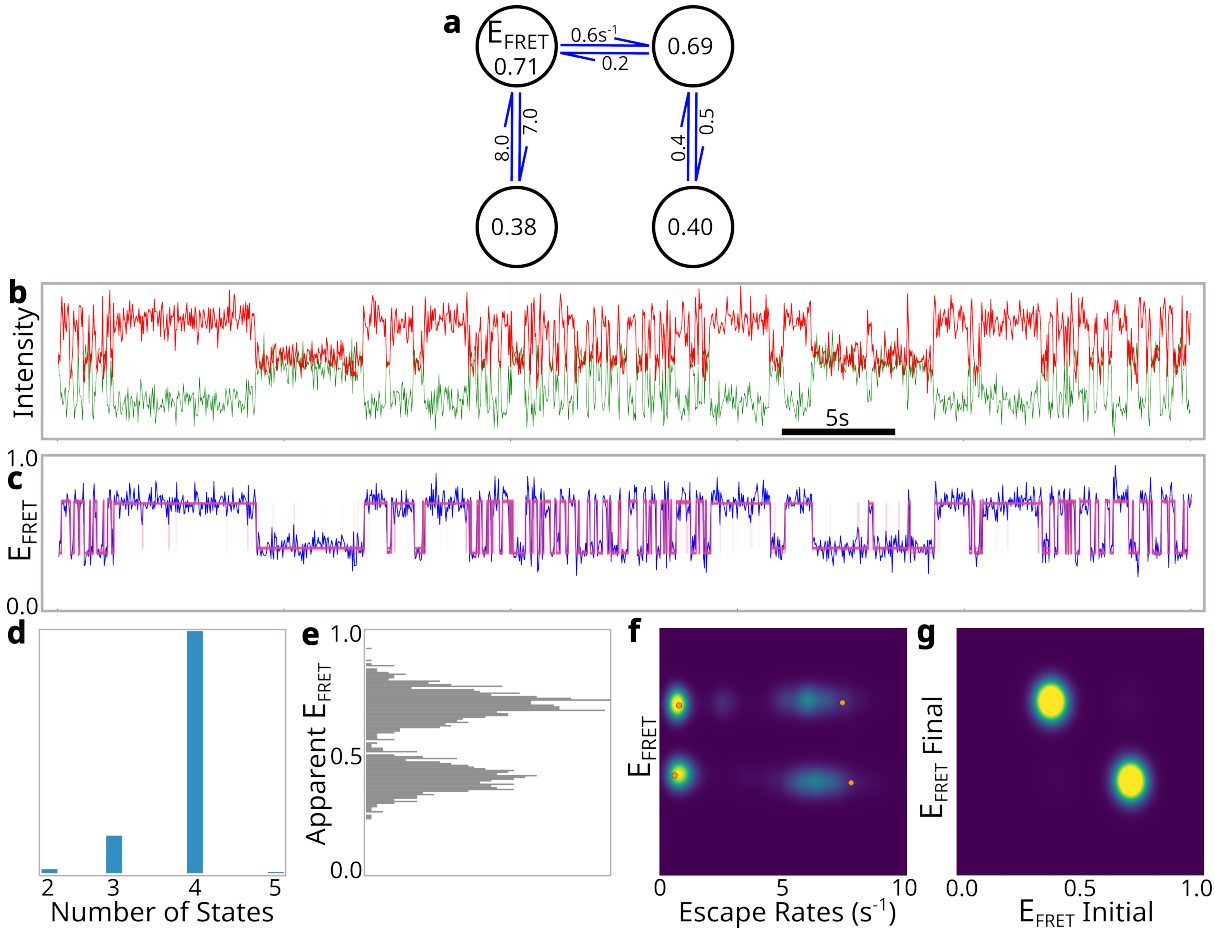

Fig. 2: BNP-FRET analysis of a simulated 4-state FRET trace with degeneracy. a. Schematic of the transition kinetics with horizontally aligned degenerate states having similar FRET efficiencies but different kinetics. **b.** FRET trace. **c.** Probability distribution over estimated state trajectories shown in pink. Apparent FRET efficiencies in blue. **d.** 4-state model is the most dominant in the histogram. **e-g.** Estimated FRET efficiencies and escape rates are close the ground truth values but due to the short length of the trace, uncertainty is higher.

These assumptions can result in multiple potential issues. First, under- or over-fitting can occur due to inaccurate estimates of noise level as already shown in Ref. [19]. Second, trace-to-trace variations in kinetics either require individually fixing the number of states for each trace, a logistically challenging task, or otherwise globally fixing the number of states for all traces that can again result in under- or over-fitting due to inaccurate identification of states. Third, flawed model selection can result from inherent inconsistencies. For example, identifying peaks from FRET efficiency histograms can result in undercounting of FRET states on account of degeneracy where states with similar FRET efficiencies cannot be distinguished. Other model selection techniques including Bayesian information criterion (BIC), Akaike information criterion (AIC), or empirical Bayes (EB) attempt to counter overfitting natural to

likelihood maximization using a penalization term [16]. Such penalties are problematic especially when data is sparse. Here, AIC/BIC may not sufficiently counter increase in likelihood due to increase in model complexity [20], or in the case of EB, estimate an overconfident or underconfident prior based on idiosyncrasies of the data itself. Furthermore, since these methods do not provide model uncertainty but only a point estimate, they can be unstable and may pick different models upon change in a few data points due to overfitting to noise, and may miss multimodal solutions where different combinations of states suit the data.

Bayesian nonparametrics (BNP) [21, 22, 23, 24], is a natural way of resolving all of the aforementioned issues—inaccurate noise modeling, fixed number of states, and lack of uncertainty estimates. In a BNP framework, the number of states itself becomes a random variable along with the other parameters of interest, kinetic rates and FRET efficiencies. Operationally, a probability distribution is estimated over an infinite-dimensional model, making BNPs infinitely flexible. A prior on the number of active/dominant model components is suitably chosen. Here, overfitting is avoided for sparse data because activation of a higher number of components is naturally suppressed by the prior unless otherwise strongly warranted by the data/likelihood. On the other hand, underfitting for sparse data is avoided by having higher uncertainty in the model estimate. Consequently, the estimated posterior reflects the quality of the data given in terms of signal-to-noise and trace length.

As such, we present BNP-FRET [25], a Julia language package that provides a complete pipeline containing: 1) a script to generate FRET traces from raw TIFF images recorded by sCMOS or EMCCD cameras; 2) a script to generate camera noise maps; and 3) an analysis tool that implements a nonparametric hidden Markov model (HMM) and generates Monte Carlo samples for all the parameters of interest. The Monte Carlo samples produced by the analysis tool for the kinetic rate matrix, FRET efficiencies, and state trajectories are stored in a single HDF5 file corresponding to each trace. We also provide a script to combine all the samples together to generate probability and transition density heatmaps.

To demonstrate the performance of BNP-FRET, we first generated a simulated FRET trace with three states and no degeneracy among the FRET states, as shown in Fig. 1a-b. We assume an sCMOS camera model where Poisson-distributed photons are incident at each pixel, and then read-out electronics add Gaussian noise to that signal. We choose realistic values for donor and acceptor emission rates, and background. As shown in Fig. 1c-g, our BNP-FRET Monte Carlo sampler finds the ground truth three-state model to be the most probable one but also estimates significant possibility for four- and five-state models, a hallmark of our method. Such higher model uncertainty arises due to medium signal-to-noise ratio, and fewer dwells in the highest and the lowest FRET states, thereby increasing sparsity in the data and uncertainty in the estimates. As an added benefit of our effort to reduce computational cost (see Methods), we also end up sampling the state trajectories, that closely match with the apparent FRET signal.

Next, we simulate a trace with degeneracy in the FRET efficiency. As shown in the kinetic diagram in Fig. 2a, states 1 & 2 and states 3 & 4 have similar FRET efficiencies, respectively. Therefore, kinetic heterogeneity, that is, different transition rates between the same pair of FRET efficiencies, is the only way to distinguish the degenerate states. If we naively use the FRET efficiency histogram peaks to estimate the number of states, we only see two states. However, estimating kinetics using two states would average the rates, resulting in under- and over- fitting in the state trajectory. BNP-FRET on the other hand explores a large number of candidate models with different dimensions that match the kinetic heterogeneity, and is correctly able to identify switching between degenerate FRET states as well the associated kinetic rates, as shown in Fig. 2c-g.

Finally, we apply BNP-FRET to hundreds of experimental FRET traces obtained from observing DNA Holliday junctions under tension using the DNA origami-based MAESTRO (Multi-axial entropic spring tweezer along a rigid origami) setup [26]. Under tension-free conditions, Holliday junctions are known to have two long-lived stacked conformations that switch at approximately the same kinetic rates [27] as shown in Fig. 3a-c. However, under four-way tension as shown in Fig. 3d, trace-to-trace variations in asymmetrically directed forces result in a wide distribution over rates with Holliday junctions prone to temporarily getting stuck in one of the two stacked conformations, as evident from dominant slow rates at low FRET efficiency in the plots in Fig. 3e. Furthermore, thermal fluctuations cause the tension forces to change directions. Consequently, Holliday junctions undergo changes in kinetic behavior during the observation period itself as shown in Fig. 3f-g, where BNP-FRET clearly predicts more than two states

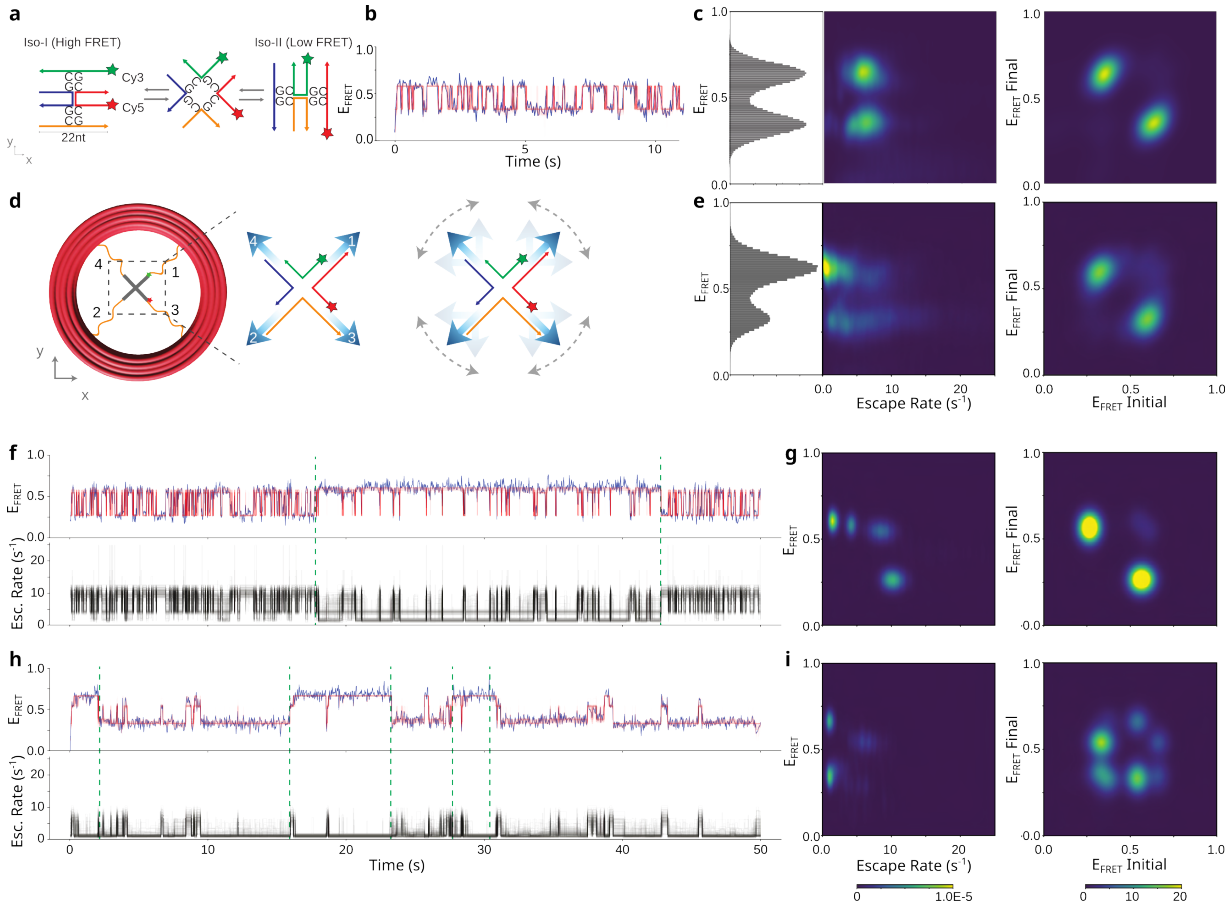

Fig. 3: Holliday junctions under tension using BNP-FRET. a. Holliday junctions typically switch between two stacked conformations via a short-lived intermediate open conformation. **b.** A typical FRET trace under tension-free conditions. FRET signal is shown in blue. BNP-FRET generated distribution for trajectories is shown in red. **c.** On the left, we have FRET efficiency histogram showing equal residence time in both conformations. The middle plot shows probability density as a function of FRET efficiency and kinetic rates demonstrating that the two conformations have similar forward and backward rates of approximately $5s^{-1}$. The plot on the right shows transition densities based on trajectories estimated by BNP-FRET. The heatmap plots are generated from over 150 traces. **d.** MAESTRO system consists of a cylindrical DNA origami to which Holliday junctions can be connected using multiple ssDNA springs that apply four-way entropic tension. Due the thermal fluctuations, these forces may change directions. **e.** Similar plots as in c but are generated using over 150 traces. Now, under tension, Holliday junctions have a high tendency to get stuck in the low FRET conformation resulting in slow escape rates out of the low FRET conformation. **f.** An example FRET trace under four-way tension where kinetics change during the observation period due to changes in the directions of the forces. The dashed lines mark the changes in kinetic behavior. BNP-FRET estimated trajectories in red fit the FRET signal well. **g.** Multiple degenerate states now show up in the FRET efficiency vs escape rate probability distribution. **h.** Another example trace but now the kinetics are much slower than the trace in f. **i.** The intermediate open conformation with intermediate FRET efficiency is now distinctly evident in the probability density heatmaps.

and resolves the degeneracy. Moreover, tension can also cause the Holliday junction to spend more time in the intermediate open conformation with intermediate FRET efficiency as shown in Fig. 3h-i. BNP-FRET is able to see this additional state. The trace-to-trace variations in the kinetics of the Holliday junctions imply that the number of states cannot be fixed globally for all traces, and otherwise, analysis of hundreds of FRET traces by individually fixing a number of states using FRET efficiency histograms or the BIC criterion would suffer from under- and overfitting, as mentioned earlier.

In conclusion, kinetic heterogeneity in biomolecules is inevitable due to their rugged energy landscapes [28, 29, 30]—even in a simple system like the Holliday junction where we observe molecules interconverting between distinct kinetic patterns. BNP-FRET is a powerful tool for analyzing such systems, particularly when dealing with degenerate FRET—cases where molecules exhibit similar FRET efficiencies but display completely different kinetics. Moreover, BNP-FRET is a rigorous and physically motivated analysis tool for studying the dynamics of biomolecules. It has significant advantages over other methods in terms of requiring minimal user input, no training time, unlike supervised methods, accurate estimation of noise, and rigorous model selection as warranted by the limited amount of data.

Methods

BNP-FRET software assumes a nonparametric hidden Markov model (HMM) structure to describe the time evolution of biomolecules through an infinite collection of states $\boldsymbol{\sigma} = \{\sigma_1, \sigma_2, \ldots\}$ at a discrete set of equally-spaced time points $\mathbf{t} = \{t_0, t_1, t_2, \ldots, t_N\}$ [24]. Transitions are assumed to only occur at these time points and the fixed state during a time bin (t_{n-1}, t_n) is labeled s_n. Transition kinetics among the states are governed by a master equation and dwell times in any state are exponentially distributed. As such, BNP-FRET is designed to produce a nonparametric probability distribution, termed posterior, over an infinite collection of binary variables $\mathbf{b} = \{b_1, b_2, \ldots\}$ that activate/deactivate states, infinite-dimensional transition rate matrix $\mathbf{G}$ governing the kinetics of the biomolecules, and an infinite collection of FRET efficiencies $\mathbf{E}^{FRET}$. Here, the nonparametric transition rate matrix $\mathbf{G}$ can be written as

$$\mathbf{G} = \begin{bmatrix} * & b_1 b_2 \lambda_{\sigma_1 \to \sigma_2} & b_1 b_3 \lambda_{\sigma_1 \to \sigma_3} & \cdots \\ b_1 b_2 \lambda_{\sigma_2 \to \sigma_1} & * & b_2 b_3 \lambda_{\sigma_2 \to \sigma_3} & \cdots \\ b_1 b_3 \lambda_{\sigma_3 \to \sigma_1} & b_2 b_3 \lambda_{\sigma_3 \to \sigma_2} & * & \cdots \\ \vdots & \vdots & \vdots & \ddots \quad \vdots \end{bmatrix}, \tag{1}$$

where $b_i \in [0, 1]$ and $\lambda_{\sigma_i \to \sigma_j}$ are rates for transition from state σ_i to σ_j. Following Bayes' rule, we compute the posterior distribution as the product of the likelihood of FRET observations $\boldsymbol{w} = \{w_1, w_2, \ldots, w_N\}$ and appropriately chosen prior probability distributions as

$$p(\mathbf{b}, \mathbf{G}, \mathbf{E}^{FRET} | \boldsymbol{w}) \propto L(\boldsymbol{w} | \mathbf{b}, \mathbf{G}, \mathbf{E}^{FRET})\, p(\mathbf{G}) p(\mathbf{b}) p(\mathbf{E}^{FRET}). \tag{2}$$

We can express the first term on the right in the proportionality above, the likelihood, for a finite set of states [31] by observing the evolution of the state probability row-vector $\boldsymbol{\rho}$ through all the time points as

$$L(\boldsymbol{w} | \mathbf{b}, \mathbf{G}, \mathbf{E}^{FRET}) \approx \boldsymbol{\rho}_{ss}\, \boldsymbol{\Pi}_1\, \boldsymbol{\Pi}_2\, \boldsymbol{\Pi}_3\, \ldots\, \boldsymbol{\Pi}_N\, \boldsymbol{\rho}_{norm}^T, \tag{3}$$

where we assume steady-state at the beginning of the FRET trace and compute the initial row-vector $\boldsymbol{\rho}_{ss}$ by setting $\boldsymbol{\rho}_{ss}\mathbf{G} = 0$. Furthermore, $\boldsymbol{\Pi}_n \equiv (\boldsymbol{\Pi} \odot \mathbf{D}_n)$ involves an element-by-element product of the transition probability matrix

$$\boldsymbol{\Pi} = \mathbf{exp}(\delta \mathbf{G}) = \begin{bmatrix} \pi_{\sigma_1 \to \sigma_1} & \pi_{\sigma_1 \to \sigma_2} & \pi_{\sigma_1 \to \sigma_3} & \cdots \\ \pi_{\sigma_2 \to \sigma_1} & \pi_{\sigma_2 \to \sigma_2} & \pi_{\sigma_2 \to \sigma_3} & \cdots \\ \pi_{\sigma_3 \to \sigma_1} & \pi_{\sigma_3 \to \sigma_2} & \pi_{\sigma_3 \to \sigma_3} & \cdots \\ \vdots & \vdots & \vdots & \ddots \quad \vdots \end{bmatrix}, \tag{4}$$

computed for a time bin of size δ and the measurement probability matrix whose elements are given by

$$(\mathbf{D}_n)_{\sigma_i \to \sigma_j} \approx p(w_n | \sigma_i), \tag{5}$$

assuming the state remains fixed during the time bin as shown in [31].

Now, computing these measurement probabilities above is challenging because of the many unobserved random variables that must be integrated over at each step noise is added to the FRET data. For example, when using sCMOS cameras, photon shot noise is added first and then Gaussian noise is added to the signal at readout [32]. Therefore, unobserved donor and acceptor photon emissions must be integrated over. In the case of EMCCD cameras, an intermediate electron multiplication stage also adds Gamma distributed noise [33], requiring us to integrate over the multiplied electronic signal. More formally, unobserved random variables that must be integrated over include number of laser photons absorbed by the donor λ_n^{abs} in each time bin which is related to the average excitation rate λ^{ex}, donor and acceptor channel photon emissions per time bin, γ_n^d and γ_n^a, respectively, and multiplied electrons in the donor and acceptor channels per time bin, e_n^d and e_n^a, respectively, if an EMCCD camera is used. That is, in case of sCMOS cameras,

$$p(w_n|s_n) = \sum_{\lambda_n^{abs}=0}^{\infty} \sum_{\gamma_n^d=0}^{\infty} \sum_{\gamma_n^a=0}^{\infty} p(w_n|\gamma_n^d, \gamma_n^a)\, p(\gamma_n^d, \gamma_n^a|\lambda_n^{abs}, s_n)\, p(\lambda_n^{abs}|\lambda^{ex}). \tag{6}$$

These integrations are not easily amenable to analytical computations and therefore we integrate by Monte Carlo. We use Markov chain Monte Carlo (MCMC) techniques such as Gibbs sampling to iteratively and sequentially generate samples for each parameter from their corresponding conditional posterior distributions. Furthermore, while the likelihood above integrates over all possible state trajectories, computational cost associated with large number of matrix exponentials can be very high. Therefore, we avoid repeatedly computing the whole likelihood to sample each parameter of interest by sampling the state trajectory $\boldsymbol{s} = \{s_1, s_2, \ldots, s_N\}$ itself. The de-marginalized complete likelihood can then be calculated as

$$\begin{aligned} L^{dem} &\equiv p(\boldsymbol{w}|\mathbf{b}, \mathbf{G}, \mathbf{E}^{FRET}, \boldsymbol{s}, \boldsymbol{\lambda}^{abs}, \boldsymbol{\gamma}^d, \boldsymbol{\gamma}^a) \\ &= \prod_{n=1}^{N} p(\lambda_n^{abs}|\lambda^{ex})\, p(\gamma_n^d, \gamma_n^a|\lambda_n^{abs}, s_n)\, p(w_n|\gamma_n^d, \gamma_n^a), \text{ or} \end{aligned} \tag{7}$$

in the case of EMCCD cameras,

$$\begin{aligned} L^{dem} &\equiv p(\boldsymbol{w}|\mathbf{b}, \mathbf{G}, \mathbf{E}^{FRET}, \boldsymbol{s}, \boldsymbol{\lambda}^{abs}, \boldsymbol{\gamma}^d, \boldsymbol{\gamma}^a, \boldsymbol{e}^d, \boldsymbol{e}^a) \\ &= \prod_{n=1}^{N} p(\lambda_n^{abs}|\lambda^{ex})\, p(\gamma_n^d, \gamma_n^a|\lambda_n^{abs}, s_n)\, p(e_n^d, e_n^a|\gamma_n^d, \gamma_n^a)\, p(w_n|e_n^d, e_n^a), \end{aligned} \tag{8}$$

where

$$p(\lambda_n^{abs}|\lambda^{ex}) = \mathbf{Poisson}(\lambda_n^{abs}; \lambda^{ex}), \tag{9}$$

$$\begin{aligned} p(\gamma_n^d, \gamma_n^a|\lambda_n^{abs}, s_n) = \mathbf{Multinomial}\big(&\gamma_n^d, \gamma_n^a; \lambda_n^{abs}, [(1 - E^{FRET}(s_n)) * Q_d,\ E^{FRET}(s_n) * Q_a, \\ &1 - (1 - E^{FRET}(s_n)) * Q_d - E^{FRET}(s_n) * Q_a]\big), \end{aligned} \tag{10}$$

$$p(w_n|\gamma_n^d, \gamma_n^a) = \mathbf{Normal}\left((d_n - o^d)/g_{ADC}; \gamma_n^d, v^d\right) \mathbf{Normal}\left((a_n - o^a)/g_{ADC}; \gamma_n^a, v^a\right), \tag{11}$$

$$p(e_n^d, e_n^a|\gamma_n^d, \gamma_n^a) = \mathbf{Gamma}\left(e_n^d; \frac{\gamma_n^d}{ENF}, ENF * g_{EM}\right) \mathbf{Gamma}\left(e_n^a; \frac{\gamma_n^a}{ENF}, ENF * g_{EM}\right), \text{ and} \tag{12}$$

$$p(w_n|e_n^d, e_n^a) = \mathbf{Normal}\left((d_n - o^d)/g_{ADC}; e_n^d, v^d\right) \mathbf{Normal}\left((a_n - o^a)/g_{ADC}; e_n^a, v^a\right), \tag{13}$$

where o^d and o^a are bias offsets for the donor and acceptor channnels, respectively, g_{ADC} and g_{EM} are analog-to-digital conversion factor and electron multiplier gain, respectively, and Q_a and Q_d are quantum yields of donor and acceptor, respectively. Furthermore, due to the stochastic nature of electron multiplication itself in EMCCD cameras, the excess noise factor, $ENF = 2.0 - 1/g_{EM}$, affects the electron multiplication significantly when gain is high and readout noise becomes relatively negligible.

To conclude, after appropriately initializing all the variables, the following Gibbs sampling strategy is employed in BNP-FRET to generate samples:

1. Truncate the infinite-dimensional model for computational reasons only to have a finite but large number of states M^{max}. Then jointly sample loads and state trajectory to avoid inconsistency between the active states and states being explored in the trajectory. To accomplish this, two trajectories corresponding to the two values of the binary variable b_i are proposed $\boldsymbol{s}_{b_i=0}$ and $\boldsymbol{s}_{b_i=1}$ using the forward filtering backward sampling algorithm [24] as

$$\boldsymbol{s}_{b_i=0} \sim p(\boldsymbol{s}|\mathbf{b}, \mathbf{G}_{b_i=0}), \text{ and} \tag{14}$$
$$\boldsymbol{s}_{b_i=1} \sim p(\boldsymbol{s}|\mathbf{b}, \mathbf{G}_{b_i=1}), \tag{15}$$

where we have ignored variables that do not directly inform the trajectories. Likelihoods are then computed for both trajectories and then conditional posteriors are computed using the Bernoulli prior for b_i as

$$p(b_i = 0|\mathbf{b}\backslash b_i, \boldsymbol{s}_{b_i=0}, \mathbf{G}, \mathbf{E}^{FRET}, \lambda^{abs}, \boldsymbol{\gamma}^d, \boldsymbol{\gamma}^a, \boldsymbol{w}) \propto L^{dem}\, p(b_i = 0), \text{ and} \tag{16}$$
$$p(b_i = 1|\mathbf{b}\backslash b_i, \boldsymbol{s}_{b_i=1}, \mathbf{G}, \mathbf{E}^{FRET}, \lambda^{abs}, \boldsymbol{\gamma}^d, \boldsymbol{\gamma}^a, \boldsymbol{w}) \propto L^{dem}\, p(b_i = 1) \tag{17}$$

where the prior with expected number of states M^{exp} is given as

$$p(b_i) = \textbf{Bernoulli}\left(b_i; \frac{1}{1 + \frac{M^{max}-1}{M^{exp}}}\right), \tag{18}$$

and suppresses activation of new states with the probability shown after the semi-colon to avoid over-fitting. For typical FRET traces, we find $M^{max} = 20$ and $M^{exp} = 2$ works well. The new value of b_i can now be sampled from a Categorical distribution as

$$\begin{aligned} b_i \sim \textbf{Categorical}_{[0,1]}\big([&p(b_i = 0|\mathbf{b}\backslash b_i, \boldsymbol{s}_{b_i=0}, \mathbf{G}, \mathbf{E}^{FRET}, \lambda^{abs}, \boldsymbol{\gamma}^d, \boldsymbol{\gamma}^a, \boldsymbol{w}), \\ &p(b_i = 1|\mathbf{b}\backslash b_i, \boldsymbol{s}_{b_i=1}, \mathbf{G}, \mathbf{E}^{FRET}, \lambda^{abs}, \boldsymbol{\gamma}^d, \boldsymbol{\gamma}^a, \boldsymbol{w})]\big), \end{aligned} \tag{19}$$

and the trajectory associated with the sampled value of b_i is accepted as the new trajectory.

2. Sample kinetic rates

$$\mathbf{G} \sim p(\mathbf{s}|\mathbf{G})p(\mathbf{G}), \tag{20}$$

where

$$p(\mathbf{s}|\mathbf{G}) = \prod_{n=1}^{N} \pi_{s_{n-1}\to s_n}, \tag{21}$$

since only the kinetic rates affect the state trajectory. Furthermore, the prior $p(\mathbf{G})$ can be chosen as a product of Gamma distributions over each rate to enforce positivity.

3. Sample FRET efficiencies

$$\mathbf{E}^{FRET} \sim L^{dem} p(\mathbf{E}^{FRET}), \tag{22}$$

where Beta distributions can be used a priors to enforce the finiteness of the domain, $E_i^{FRET} \in (0, 1)$

4. Sample donor excitation rate

$$\lambda^{ex} \sim L^{dem} p(\lambda^{ex}), \tag{23}$$

where Gamma distribution can be used for the prior to enforce positivity.

5. Sample donor photon absorptions

$$\lambda_n^{abs} \sim p(\gamma_n^d, \gamma_n^a|\lambda_n^{abs}, s_n)\, p(\lambda_n^{abs}|\lambda^{ex}). \tag{24}$$

6. Sample donor and acceptor emissions

$$\gamma_n^d, \gamma_n^a \sim p(w_n|\gamma_n^d, \gamma_n^a)\, p(\gamma_n^d, \gamma_n^a|\lambda_n^{abs}, s_n). \tag{25}$$

7. Sample multiplied electrons in donor and acceptor channels (in the case of EMCCD cameras)

$$e_n^d, e_n^a \sim p(w_n|e_n^d, e_n^a)\, p(e_n^d|\gamma_n^d)\, p(e_n^a|\gamma_n^a). \tag{26}$$

In cases where the conditional posteriors are not amenable to direct sampling, we employ techniques such as Metropolis-Hastings to generate samples. Once enough uncorrelated MCMC samples have been collected, they can be used to compute statistical quantities such as mean, uncertainties, and confidence intervals if desired.

Acknowledgments

RFH acknowledges support form the National Science Foundation (NSF) through NSF career (MCB 2341002). SP acknowledges support from the National Institutes of Health (NIH) (R01GM134426, R01GM130745, R35GM148237), and US Army (ARO (W911NF-23-1-0304)). GBMW is supported by an American Heart Association (AHA) predoctoral fellowship (23PRE1029870). We acknowledge the use of facilities within the Eyring Materials Center as well as Phoenix and Sol supercomputers at Arizona State University.

References

[1] Luling Wu, Chusen Huang, Ben P Emery, Adam C Sedgwick, Steven D Bull, Xiao-Peng He, He Tian, Juyoung Yoon, Jonathan L Sessler, and Tony D James. Förster resonance energy transfer (FRET)-based small-molecule sensors and imaging agents. *Chemical Society Reviews*, 49:5110, 2020.

[2] Rahul Roy, Sungchul Hohng, and Taekjip Ha. A practical guide to single-molecule FRET. *Nature Methods*, 5:507, 2008.

[3] Alexander P Demchenko. *Introduction to fluorescence sensing*. Springer Science & Business Media, 2008.

[4] Ammasi Periasamy and Richard Day. *Molecular imaging: FRET microscopy and spectroscopy*. Elsevier, 2011.

[5] Elizabeth Rhoades, Eugene Gussakovsky, and Gilad Haran. Watching proteins fold one molecule at a time. *Proceedings of the National Academy of Sciences*, 100:3197, 2003.

[6] Boris Martinac. Single-molecule FRET studies of ion channels. *Progress in Biophysics and Molecular Biology*, 130:192, 2017.

[7] Hoi Sung Chung, Kevin McHale, John M. Louis, and William A. Eaton. Single-molecule fluorescence experiments determine protein folding transition path times. *Science*, 335:981, 2012.

[8] S Pressé, K Ghosh, R Phillips, and KA Dill. Dynamical fluctuations in biochemical reactions and cycles. *Physical Review E*, 82:031905, 2010.

[9] Benjamin Schuler. Single-molecule FRET of protein structure and dynamics - a primer. *Journal of Nanobiotechnology*, 11:S2, 2013.

[10] Oana Coban, Laura C Zanetti-Dominguez, Daniel R Matthews, Daniel J Rolfe, Gregory Weitsman, Paul R Barber, Jody Barbeau, Viviane Devauges, Florian Kampmeier, Martyn Winn, et al. Effect of phosphorylation on EGFR dimer stability probed by single-molecule dynamics and FRET/FLIM. *Biophysical Journal*, 108:1013, 2015.

[11] Kangkan Halder, Nicole Dölker, Qui Van, Ingo Gregor, Achim Dickmanns, Imke Baade, Ralph H Kehlenbach, Ralf Ficner, Jörg Enderlein, Helmut Grubmüller, et al. MD simulations and FRET reveal an environment-sensitive conformational plasticity of importin-β. *Biophysical Journal*, 109:277, 2015.

[12] Tara Sabir, Gunnar F. Schröder, Anita Toulmin, Peter McGlynn, and Steven W. Magennis. Global structure of forked DNA in solution revealed by high-resolution single-molecule FRET. *Journal of the American Chemical Society*, 133:11881191, 2011.

[13] Carey Phelps, Brett Israels, Davis Jose, Morgan C. Marsh, Peter H. von Hippel, and Andrew H. Marcus. Using microsecond single-molecule FRET to determine the assembly pathways of T4 ssDNA binding protein onto model DNA replication forks. *Proceedings of the National Academy of Sciences*, 114:E3612, 2017.

[14] Laura E. Baltierra-Jasso, Michael J. Morten, Linda Laflör, Steven D. Quinn, and Steven W. Magennis. Crowding-induced hybridization of single DNA hairpins. *Journal of the American Chemical Society*, 137:16020, 2015.

[15] Markus Götz and et al. A blind benchmark of analysis tools to infer kinetic rate constants from single-molecule FRET trajectories. *Nature Communications*, 13:5402, 2022.

[16] Daniel Nettels, Nicola Galvanetto, Miloš T Ivanović, Mark Nüesch, Tianjin Yang, and Benjamin Schuler. Single-molecule FRET for probing nanoscale biomolecular dynamics. *Nature Reviews Physics*, 6:587, 2024.

[17] Simon Wanninger, Pooyeh Asadiatouei, Johann Bohlen, Clemens-Bässem Salem, Philip Tinnefeld, Evelyn Ploetz, and Don C Lamb. Deep-lasi: deep-learning assisted, single-molecule imaging analysis of multi-color DNA origami structures. *Nature Communications*, 14:6564, 2023.

[18] Johannes Thomsen, Magnus Berg Sletfjerding, Simon Bo Jensen, Stefano Stella, Bijoya Paul, Mette Galsgaard Malle, Guillermo Montoya, Troels Christian Petersen, and Nikos S Hatzakis. DeepFRET, a software for rapid and automated single-molecule fret data classification using deep learning. *Elife*, 9:e60404, 2020.

[19] Ayush Saurabh, Lance W. Q. Xu, and Steve Pressé. On the statistical foundation of a recent single molecule fret benchmark. *Nature Communications*, 15:3627, 2024.

[20] Argha Bandyopadhyay and Marcel P Goldschen-Ohm. Unsupervised selection of optimal single-molecule time series idealization criterion. *Biophysical Journal*, 120:4472, 2021.

[21] Keegan E Hines, John R Bankston, and Richard W Aldrich. Analyzing single-molecule time series via nonparametric Bayesian inference. *Biophysical Journal*, 108:540, 2015.

[22] Ioannis Sgouralis, Shreya Madaan, Franky Djutanta, Rachael Kha, Rizal F. Hariadi, and Steve Pressé. A Bayesian nonparametric approach to single molecule Förster resonance energy transfer. *The Journal of Physical Chemistry B*, page 675, 2019.

[23] Ioannis Sgouralis and Steve Pressé. An introduction to infinite HMMs for single-molecule data analysis. *Biophysical Journal*, 112:2021, 2017.

[24] Steve Pressé and Ioannis Sgouralis. *Data modeling for the sciences: applications, basics, computations*. Cambridge University Press, 2023.

[25] `https://github.com/LabPresse/BNP-FRET-Binned`.

[26] Gde Bimananda Mahardika Wisna, Ayush Saurabh, Ranjan Sasmal, Deepak Karna, Prathamesh Chopade, Steve Presse, and Rizal F Hariadi. DNA origami-based platform for multi-axial single-molecule force spectroscopy reveals hidden dynamics in Holliday junctions. *bioRxiv*, pages 2025–06, 2025.

[27] Sean A McKinney, Anne-Cécile Déclais, David MJ Lilley, and Taekjip Ha. Structural dynamics of individual Holliday junctions. *Nature Structural Biology*, 10(2):93, 2003.

[28] Christoph Manz, Andrei Yu Kobitski, Ayan Samanta, Bettina G Keller, Andres Jäschke, and G Ulrich Nienhaus. Single-molecule FRET reveals the energy landscape of the full-length SAM-I riboswitch. *Nature Chemical Biology*, 13:1172, 2017.

[29] Sergey V Solomatin, Max Greenfeld, Steven Chu, and Daniel Herschlag. Multiple native states reveal persistent ruggedness of an RNA folding landscape. *Nature*, 463:681, 2010.

[30] Benjamin Schuler and Hagen Hofmann. Single-molecule spectroscopy of protein folding dynamics—expanding scope and timescales. *Current Opinion in Structural Biology*, 23:36, 2013.

[31] Ayush Saurabh, Mohamadreza Fazel, Matthew Safar, Ioannis Sgouralis, and Steve Pressé. Single-photon smFRET. I: Theory and conceptual basis. *Biophysical Reports*, 3, 2023.

[32] Biagio Mandracchia, Xuanwen Hua, Changliang Guo, Jeonghwan Son, Tara Urner, and Shu Jia. Fast and accurate sCMOS noise correction for fluorescence microscopy. *Nature Communications*, 11:1, 2020.

[33] Michael Hirsch, Richard J Wareham, Marisa L Martin-Fernandez, Michael P Hobson, and Daniel J Rolfe. A stochastic model for electron multiplication charge-coupled devices–from theory to practice. *PLOS ONE*, 8:1, 2013.